Estimation of damped oscillation associated spectra from ultrafast transient absorption spectra

Ivo H. M. van Stokkum,[1,a)] Chanelle C. Jumper,[2] Joris J. Snellenburg,[1]
Gregory D. Scholes,[3] Rienk van Grondelle,[1] and Pavel Malý[1,4]
[1]*Institute for Lasers, Life and Biophotonics, Faculty of Sciences, Vrije Universiteit Amsterdam, De Boelelaan 1081, 1081 HV Amsterdam, The Netherlands*
[2]*Department of Chemistry, University of Toronto, Toronto, Ontario M5S 3H6, Canada*
[3]*Department of Chemistry, Princeton University, Princeton, New Jersey 08544, USA*
[4]*Institute of Physics, Charles University, Prague 12116, Czech Republic*

(Received 22 July 2016; accepted 13 October 2016; published online 2 November 2016)

When exciting a complex molecular system with a short optical pulse, all chromophores present in the system can be excited. The resulting superposition of electronically and vibrationally excited states evolves in time, which is monitored with transient absorption spectroscopy. We present a methodology to resolve simultaneously the contributions of the different electronically and vibrationally excited states from the complete data. The evolution of the excited states is described with a superposition of damped oscillations. The amplitude of a damped oscillation $\cos(\omega_n t)\exp(-\gamma_n t)$ as a function of the detection wavelength constitutes a damped oscillation associated spectrum $DOAS_n(\lambda)$ with an accompanying phase characteristic $\varphi_n(\lambda)$. In a case study, the cryptophyte photosynthetic antenna complex PC612 which contains eight bilin chromophores was excited by a broadband optical pulse. Difference absorption spectra from 525 to 715 nm were measured until 1 ns. The population dynamics is described by four lifetimes, with interchromophore equilibration in 0.8 and 7.5 ps. We have resolved 24 DOAS with frequencies between 130 and 1649 cm^{-1} and with damping rates between 0.9 and 12 ps^{-1}. In addition, 11 more DOAS with faster damping rates were necessary to describe the "coherent artefact." The DOAS contains both ground and excited state features. Their interpretation is aided by DOAS analysis of simulated transient absorption signals resulting from stimulated emission and ground state bleach. [http://dx.doi.org/10.1063/1.4966196]

INTRODUCTION

Transient absorption spectroscopy is widely used to follow photophysical dynamics in systems ranging from relatively simple molecular systems[1–7] to complex photosynthetic assemblies.[8–14] When impulsively exciting a molecule with a broadband pulse, Franck-Condon active modes can be launched (according to a semi-classical model) in the ground and excited state potential energy surfaces.[15–19] In this regime, we expect superimposed population and coherence dynamics in transient absorption spectra. Whether vibrational wavepackets are generated on the ground or excited state potential energy surfaces depends on the properties (spectrum, duration, and chirp) of the exciting pulse[4,20–24] and ground state vibrations can be suppressed by a sufficiently short broadband pulse. Vibrations can be assigned to the ground or excited state based on their amplitude and phase profiles, where a node in the amplitude, accompanied by a corresponding phase flip, marks the minimum of the electronic potential energy surface that the wavepacket is propagating on.[5–7,25–29] Vibronic coherences are relevant to the study of photosynthetic energy transfer,[25,27,30–38] photosynthetic charge separation,[39] exciton coherence,[40] electron transfer,[28] internal conversion,[2] light-activated geometry changes,[5] conical intersections,[7] photoisomerization,[1,20,29,41] photodissociation,[42,43] and coherent phonons in polymers and crystals.[44–46]

In order to investigate the dynamics revealed in transient absorption spectra, populations and oscillations are currently treated separately. First the population dynamics is fitted and subtracted from the data. Then the residual signals well after the instrument response function (IRF) duration are analyzed. Time traces at single detection wavelengths are either Fourier transformed, or fitted with damped cosines.[1,2,4,25,27,41,47] Next, for a few dominant frequencies the amplitude and phase can be plotted as function of the detection wavelength. No attempt has been made yet to globally analyze the complete data. In this paper, we present a methodology to resolve simultaneously the contributions of the different electronically and vibrationally excited states from the complete dataset in order to extend the applicability of global analysis to datasets comprising both features.

In a case study, new high quality data from the cryptophyte photosynthetic antenna complex PC612[25,48] will be analyzed. When structural information is available, the dynamics of complex molecular systems can be studied with quantum mechanical methods, and time resolved spectra can

a)Electronic mail: i.h.m.van.stokkum@vu.nl. Telephone: +31205987868.

be predicted, which has been done for the photosynthetic antenna complexes PE545[49,50] and PC577.[26] Here no structural information is used, nor quantum mechanical methods. Instead, the data are described by a parametric model, employing the global and target analysis methodology[51–53] to describe the spectral evolution of electronically excited states.

In target analysis, the inverse problem is to determine the number of electronically excited states (N_{states}) present in the system, and to estimate their spectral properties $SADS_l(\lambda)$ (species associated difference spectra) and their populations $c_l^S(t)$ (superscript S stands for species). The time resolved spectra $TRS(t,\lambda)$ are described by a parameterized superposition model

$$TRS(t,\lambda) = \sum_{l=1}^{Nstates} c_l^S(t,\theta) SADS_l(\lambda),$$

where the populations are determined by an unknown compartmental model that depends upon the unknown kinetic parameters θ. In the target analysis, constraints on the *SADS* are needed to estimate all parameters θ and $SADS_l(\lambda)$. We here describe the evolution of the vibrationally excited state wavepackets created by the short laser pulse with a superposition of damped oscillations. The amplitude of a damped oscillation $\cos(\omega_n t)\exp(-\gamma_n t)$ as a function of the detection wavelength constitutes a damped oscillation associated spectrum $DOAS_n(\lambda)$ with an accompanying phase characteristic $\varphi_n(\lambda)$. When the vibrational evolution can be considered independently from the electronic evolution (Born-Oppenheimer approximation), we arrive at a superposition of the electronic and vibrational contributions to the $TRS(t,\lambda)$,[70]

$$TRS(t,\lambda) = \sum_{l=1}^{N states} c_l^S(t',\theta) SADS_l(\lambda) + \sum_{n=1}^{Nosc} DOAS_n(\lambda) \times \cos(\omega_n t' - \varphi_n(\lambda))\exp(-\gamma_n t'),$$

where t' indicates that the actual model function still has to take into account the IRF (*vide infra*). Thus the inverse problem is now extended: to determine additionally the number of vibrationally excited states N_{osc}, and to estimate their parameters, the eigenfrequency ω_n and damping rate γ_n, and the $DOAS_n(\lambda)$ and $\varphi_n(\lambda)$. Note that it is now the system that reveals its eigenfrequencies from the complete dataset. The amount of vibrationally excited states that can reliably be resolved will critically depend upon the signal to noise ratio of the measurements $TRS(t,\lambda)$. We will demonstrate the applicability of the methodology and compare with results from published high-resolution measurements of light harvesting proteins.[25,27]

MATERIALS AND METHODS

Modelling and parameter estimation

The population of the l-th compartment is $c_l^S(t)$. The concentrations of all compartments are collated in a vector $c^S(t) = \left[c_1^S(t)\ c_2^S(t) \ldots c_{n_{comp}}^S(t)\right]^T$, which obeys the differential equation

$$\frac{d}{dt}c^S(t) = Kc^S(t) + j(t),$$

where the transfer matrix K contains off-diagonal elements k_{pq}, representing the microscopic rate constant from compartment q to compartment p. The diagonal elements contain the total decay rates of each compartment. The input to the compartments is $j(t) = IRF(t)\left[x_1 \ldots x_{n_{comp}}\right]^T$, with x_l the absorption of the l-th compartment.

The impulse response of the system, which is a sum of exponential decays, has to be convolved with the IRF. Typically, a Gaussian shaped IRF is adequate, with parameters μ for the location of the IRF maximum and Δ for the full width at half maximum (FWHM) of the IRF,

$$IRF(t) = \frac{1}{\tilde{\Delta}\sqrt{2\pi}} \exp(-\log(2)(2(t-\mu)/\Delta)^2),$$

where $\tilde{\Delta} = \Delta/(2\sqrt{2\log(2)})$. The convolution (indicated by an *) of this IRF with an exponential decay (with decay rate k) yields an analytical expression, which facilitates the estimation of the decay rate k and the IRF parameters μ and Δ,

$$\begin{aligned} c^D(t,k,\mu,\Delta) &= \exp(-kt) * IRF(t) \\ &= \frac{1}{2}\exp(-kt)\exp\left(k\left(\mu + \frac{k\tilde{\Delta}^2}{2}\right)\right) \\ &\quad \times \left\{1 + erf\left(\frac{t-(\mu + k\tilde{\Delta}^2)}{\sqrt{2}\tilde{\Delta}}\right)\right\}. \end{aligned}$$

When the compartmental model consists of independently decaying species, with populations $c_l^D(t,k_l,\mu,\Delta)$ (superscript D stands for decay) their spectra are termed $DADS_l(\lambda)$ (decay associated difference spectra). The solution of the general compartmental model described by the K matrix consists of exponential decays with decay rates equal to the eigenvalues of the K matrix. The interrelation between the DADS and SADS is expressed in the following matrix equation:

$$C^D(\theta,\mu,\Delta)\cdot DADS^T = C^S(\theta,\mu,\Delta)\cdot SADS^T.$$

Here the matrix $C^D(\theta,\mu,\Delta)$ contains in its l-th column the decay $c_l^D(t,k_l,\mu,\Delta)$ and the matrix $C^S(\theta,\mu,\Delta)$ contains in its columns the populations $c_l^S(t)$ of the general compartmental model.

The superposition model for the $TRS(t,\lambda)$ is given by the matrix formula

$$\begin{aligned} TRS = C^S(\theta,\mu,\Delta)\cdot SADS^T &+ \mathrm{Cos}(\omega,\gamma,\mu,\Delta)\cdot A^T \\ &+ \mathrm{Sin}(\omega,\gamma,\mu,\Delta)\cdot B^T. \end{aligned}$$

Here the matrices $\mathrm{Cos}(\omega,\gamma,\mu,\Delta)$ and $\mathrm{Sin}(\omega,\gamma,\mu,\Delta)$ contain the damped oscillations, which will be detailed below, and the matrices A and B comprise their amplitudes.

To improve the precision of the estimated parameters, the experiment can be repeated, and the set of N_{exp} experiments can be analyzed simultaneously. For each additional dataset TRS_e only one scaling parameter α_e and one time shift parameter μ_e must be added

$$\begin{aligned} TRS_e = \alpha_e(C^S(\theta,\mu_e,\Delta)\cdot SADS^T &+ \mathrm{Cos}(\omega,\gamma,\mu_e,\Delta)\cdot A^T \\ &+ \mathrm{Sin}(\omega,\gamma,\mu_e,\Delta)\cdot B^T). \end{aligned}$$

The dimensions of the matrices are collated in Table I.

TABLE I. Dimensions of the matrices.

	Nrow	Ncol
TRS	nt	nλ
$C^S(\theta,\mu,\Delta)$	nt	N_{states}
SADS	nλ	N_{states}
$\mathrm{Cos}(\omega,\gamma,\mu,\Delta)$	nt	N_{osc}
A	nλ	N_{osc}
$\mathrm{Sin}(\omega,\gamma,\mu,\Delta)$	nt	N_{osc}
B	nλ	N_{osc}

Assuming wavelength independence of the eigenfrequency ω_n and of the damping rate γ_n is necessary to limit the amount of free parameters. The model function for the n-th damped oscillation is given by

$$\cos(\omega_n(t-\mu))\cdot c^D(t,\gamma_n,\mu,\Delta),$$
$$\sin(\omega_n(t-\mu))\cdot c^D(t,\gamma_n,\mu,\Delta).$$

Note that we have chosen this approximate product expression in order to avoid the complications, which arise from the convolution of $c^D(t,\gamma_n,\mu,\Delta)$ with a sine or cosine function.

Using these two functions, the matrices $\mathrm{Cos}(\omega,\gamma,\mu,\Delta)$ and $\mathrm{Sin}(\omega,\gamma,\mu,\Delta)$ can be computed as a function of all ω_n,γ_n. The intrinsically nonlinear parameters of this model are the vector θ (containing the microscopic decay rates and inputs to the compartments x_l), the IRF parameters (μ,Δ), scaling parameter α_e, and time shift parameter μ_e for each additional dataset, and the N_{osc}-vectors ω,γ. The conditionally linear parameters are the matrices *SADS*, *A*, and *B*. Typically, there are nλ times more conditionally linear parameters than intrinsically nonlinear parameters, see Table I. The variable projection algorithm[52,54–56] which minimizes the nonlinear least squares criterion as a function of the intrinsically nonlinear parameters only, and implicitly solves for the conditionally linear parameters, makes the parameter estimation feasible.

The DOAS and phases cannot be fitted directly, but must be computed from the estimated cosine and sine amplitude matrices A and B. The n-th $DOAS_n$ at wavelength λ_j is computed as

$$DOAS_{jn}=\sqrt{A_{jn}^2+B_{jn}^2}.$$

The reconstruction of the phase φ_n is more cumbersome. From A_{jn} and B_{jn} the phase φ_{jn} modulo 2π can be computed. Then undesired 2π jumps between subsequent phases φ_{jn} and $\varphi_{j+1,n}$ can be corrected by applying appropriate counterjumps of 2π.

Transient absorption measurements

Transient absorption measurements of cryptophyte light harvesting proteins have been described in Refs. 25 and 27. Different from those measurements, detection here was at the magic angle, instead of parallel, which precludes depolarization effects. A typical experiment consists of nt = 959 time gated spectra measured at nλ = 650 wavelengths

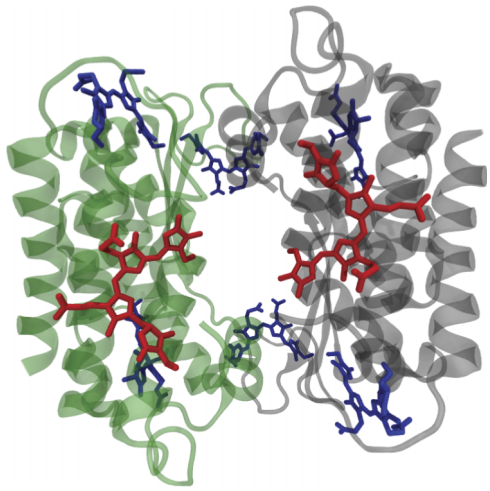

FIG. 1. Visualization of the X-ray crystal structure of the PC612 light harvesting protein,[48] which contains eight covalently bound chromophores: two dihydrobiliverdin (DBV, red), and six phycocyanobilin (PCB, blue).

(with wavelength step 0.293 nm). In the estimation of spectra there is always a balance between variance and bias. When smoothing the DADS or DOAS by averaging four consecutive wavelength points (corresponding to 1.172 nm), a small bias is introduced but the variance is expected to halve. In the main text, we present results with averaging four consecutive wavelength points. In the supporting information, we compare with the unaveraged data, cf., Figure S 1 of the supplementary material. Time-gated difference spectra were taken at equidistant time points in the first two ps (with time step of 3 fs), and with gradually increasing time steps until 1000 ps. The estimated FWHM of the IRF was 21 fs. Each experiment was repeated at least 5 times on 3 different days to confirm reproducibility.

Here we analyse data recorded for the PC612 light harvesting complex from the cryptophyte *Hemiselmis virescens* CCAC 1635 B, which contains eight covalently bound chromophores: two dihydrobiliverdin (DBV) and six phycocyanobilin (PCB), indicated in red and blue in Figure 1. PC 612 is a phycobiliprotein. Phycobiliproteins are found

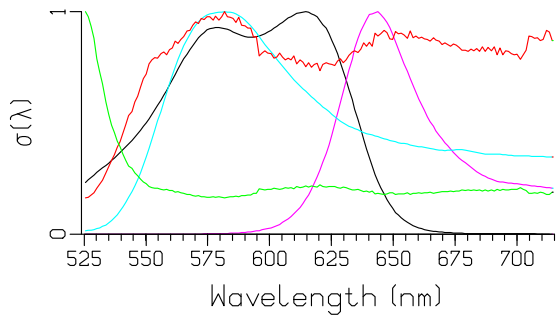

FIG. 2. Broadband excitatory pulses were tuned centrally to 580 nm with an asymmetric Lorentzian extending past 650 nm (cyan), overlapping well with the entire PC612 absorption (black) and emission spectrum (magenta). The wavelength dependence of the root mean square error (rmse) of the fit (green), scaled for comparison (rmse maximum 1.36 mOD at 525 nm, minimum 0.22 mOD at 582 nm). The reciprocal of the rmse (red) is used as the weight in the nonlinear least squares fit.

in cyanobacteria (blue-green algae), red algae, and the cryptomonads.[57]

Broadband excitation pulses were tuned centrally to 580 nm with an asymmetric Lorentzian tail extending past 650 nm, overlapping well with the entire PC612 absorption spectrum (indicated by, respectively, cyan and black lines in Figure 2), most strongly exciting the higher-energy DBV chromophores. The red curve represents the wavelength dependence of the reciprocal of the root mean square error (rmse) of the fit, which is used as a weighting factor in the nonlinear least squares fit. This weight is determined iteratively, and the curve shown here represents the best fit. The repetition rate of the excitatory pulses was 5 kHz. Thus a long lived species (e.g., a triplet or a charge-transfer state) can accumulate if its lifetime is longer than 50 μs. If its population becomes sizeable, possible annihilation processes have to be taken into account as well in the target analysis. The spectrum of this long lived species is depicted in grey in Figure S 4. It will be discussed below.

Residual analysis

Following a successfully converged fit, the matrix of residuals is analyzed with the help of a singular value decomposition (SVD). Formally, the residual matrix can be decomposed as

$$res(t,\lambda) = \sum_{l=1}^{m} u_l^{res}(t) s_l w_l^{res}(\lambda),$$

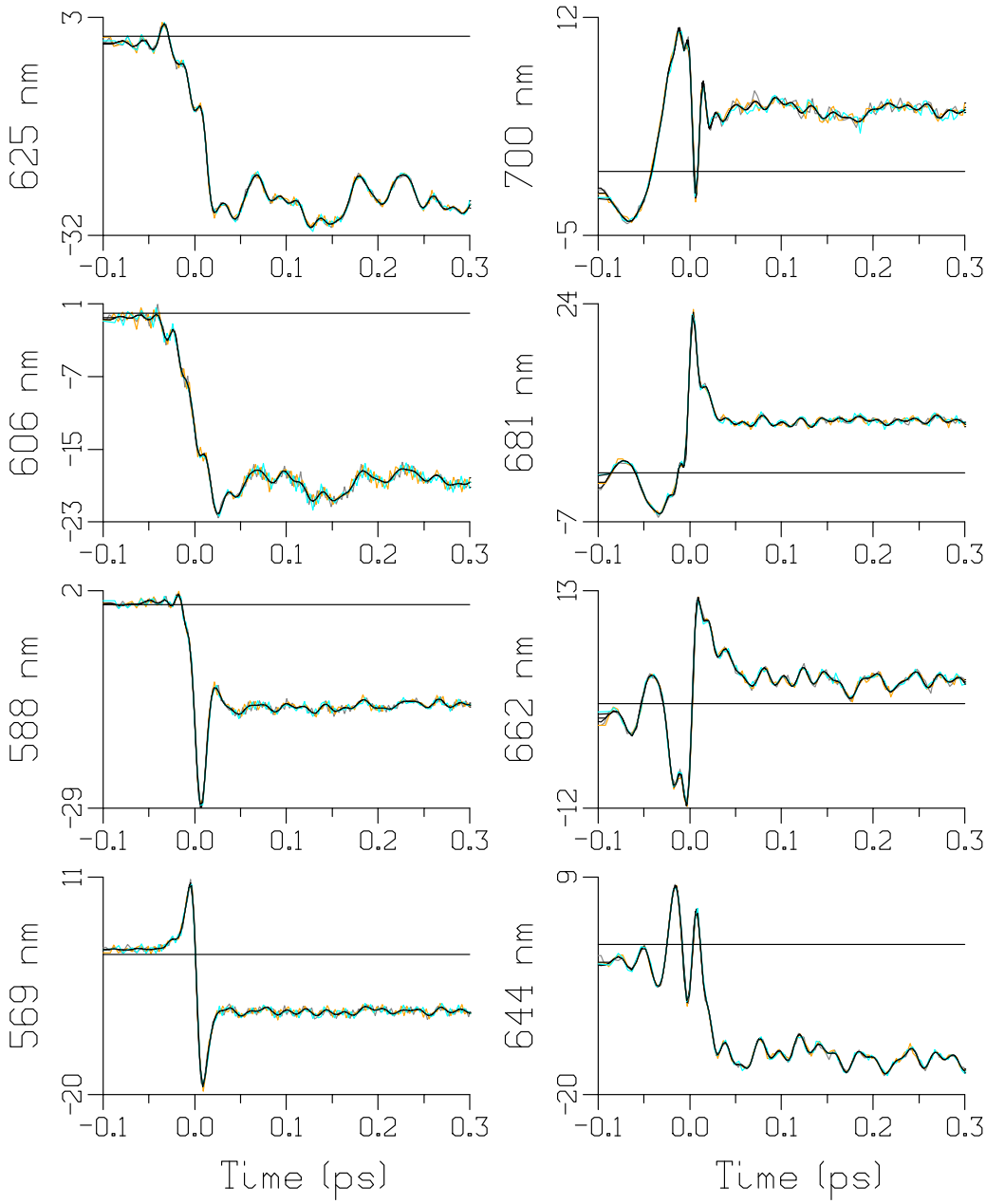

FIG. 3. Selected time traces of PC612 data (in mOD, three experiments indicated in grey, orange, and cyan) and fit (black). Wavelength is indicated in the ordinate label. Zoom from −0.1 ps to 0.3 ps (after the maximum of the IRF).

where u_l and w_l are the left and right singular vectors, s_l the sorted singular values, and m is the minimum of the number of rows and columns of the matrix. The singular vectors are orthogonal and provide an optimal least squares approximation of the matrix. The SVD of the matrix of residuals is useful to diagnose shortcomings of the model used, or systematic errors in the data. A power spectrum $P_l(\omega)$ of each of the most important left singular vectors $u_l^{res}(t)$ can be computed with the help of the FFT (for the part of the data measured at equidistant time points) or of the discrete Fourier transform (DFT), with nonequidistant time points. Typically, a peak in $P_l(\omega)$ coincides with an obvious trend in $u_l^{res}(t)$. The frequency of the peak can then provide a starting value for the frequency of an additional damped oscillation. N_{osc} can be decided upon visual inspection, from the absence of obvious trends in $u_l^{res}(t)$ and of obvious peaks in $P_l(\omega)$. When the $w_l^{res}(\lambda)$ of all $N_{\exp}$ experiments are similar, consideration of the $u_l^{res}(t)$ and $P_l(\omega)$ strengthens this procedure, since a putative additional oscillation should be present in all experiments. Thus a reliable N_{osc} can be determined. Figure S 2 demonstrates that after a global analysis with exponential decays, but without fitting the damped oscillations, the residual matrices show a common structure for all three experiments. The scree plot on the top shows an elbow around $l = 17$, which indicates that for higher values the noise will dominate. The first and second pairs of left and right singular vectors are dominated by the coherent artifact phenomena straddling time zero, showing very broad power spectra. The third and higher left singular vectors depict the long lived oscillations. Their power spectra show distinct peaks at many frequencies. Those peak frequencies can be used as starting values for the ω_n parameters of the damped oscillations. Note that the common structure for all three experiments is present until about the 17th pair of left and right singular vectors. Above that the noise that differs for each experiment starts to interfere more and more, and less common structure is visible. Thus we infer that at least 17 components that are linearly independent in both time and wavelength will be needed to describe the oscillations in the data. Note that it is impossible to infer the number of resolvable damped oscillations from this residual analysis, because the SVD cannot take into account any phase characteristic.

RESULTS

The excellent reproducibility of three independent measurements is demonstrated in Figure S 1. The problem is: what is the signal and what is the noise? Reproducible oscillations are clearly present until about 1 ps, after that a noise level of 0.51 mOD is present. Averaging over four consecutive wavelength points reduces this to a noise level of 0.29 mOD. Thus our modelling should aim to describe the signal up to this noise level. The quality of the fit is demonstrated in Figure 3 for a small selection of the data, emphasizing the early times. The residuals will be discussed below. The spectral evolution of the electronically excited states is described by four lifetimes of 0.84, 7.5, 109, and

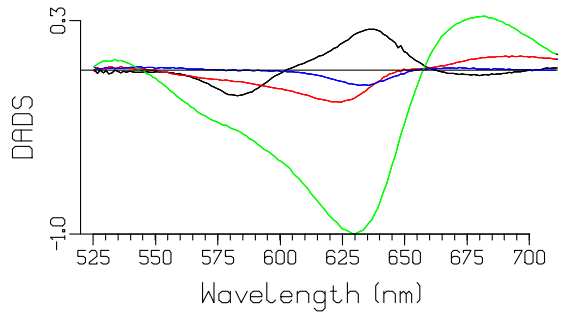

FIG. 4. Estimated DADS of PC612 after broadband excitation centered at 580 nm. Key: 0.84 (black), 7.5 (red), 109 (blue), and 1587 ps (light green).

1587 ps. The estimated DADS are depicted in Figure 4. The first DADS of 0.84 ps can be interpreted as equilibration between the more blue absorbing DBVs and the more red absorbing PCBs. This downhill energy transfer is followed by two slower steps of 7.5 and 109 ps which are less easily interpretable. Some loss of excited state as well as some further equilibration appears to be present. The final equilibrated state decays with a lifetime of 1587 ps. A target kinetic scheme with four consecutive compartments and three equilibria is depicted in Figure 5(a). By manipulating the inputs to each of the four compartments, and by adjusting the free energy differences, we arrived at the populations and SADS

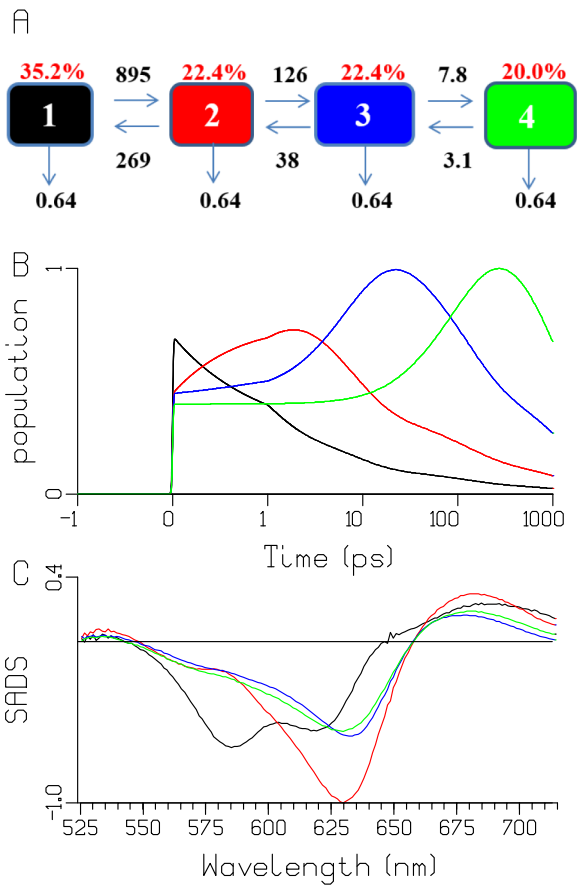

FIG. 5. (a) Kinetic scheme with microscopic rate constants (in ns^{-1}). Input fractions (red) are on top of each of the four compartments. (b) Population profiles of the four species, note that the time axis is linear until 1 ps (after the maximum of the IRF), and logarithmic thereafter. (c) Estimated SADS.

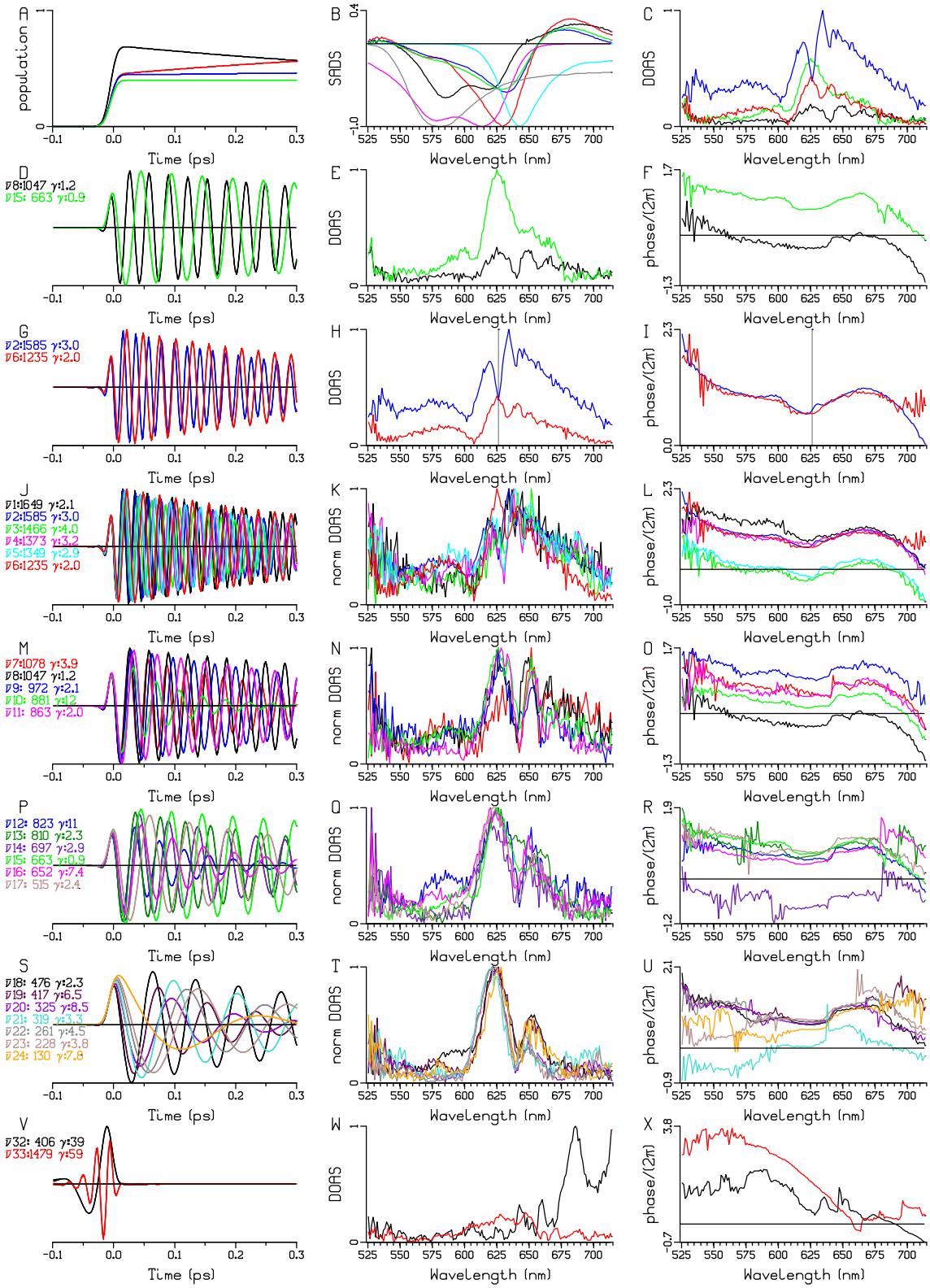

FIG. 6. Overview of the estimated DOAS and phases. (a) Species populations from Figure 5(b) depicted until 0.3 ps. The maximum of the IRF is at time zero. (b) SADS from Figure 5(c). In addition, the negative of the steady state absorption (magenta) and emission (cyan) are plotted for reference. (c) Superposition of four selected DOAS with frequencies between 663 and 1585 cm^{-1}, and damping rates between 0.9 and 3.0 ps^{-1}, which are detailed in panels (d)-(i). Row 2-8: (left column) cosine oscillations with frequencies $\bar{\nu}n$ (in cm^{-1}) (where n is the DOAS number) and damping rates γ (in 1 ps^{-1}) written in the legend at the left, using the appropriate color. (Middle column) Estimated DOAS (with number indicated in the legend at the far left), normalized (norm) for comparison. (Right column) Estimated phase profiles of the DOAS. The grey vertical lines at 626.5 nm in panels (h) and (i) are discussed in the text.

depicted in Figures 5(b) and 5(c). The first compartment (colored black) represents the blue absorbing DBVs. The DBV SADS shows minima at ≈585 and ≈620 nm, due to bleaching and stimulated emission.[58] In addition, excited state absorption (ESA) is present at ≈680 nm. The other three SADS exhibit bleaching and stimulated emission at 630-640 nm,

and ESA at ≈680 nm. They represent the six PCB chromophores.

Thirty-five damped oscillations were needed to fit the vibrational evolution up to the noise level, cf., Figures S 5 and S 6. The first left and right singular vectors of the residual matrix are depicted in Figures S 7 and S 8. No obvious structure that is consistent for the three experiments is discernible. Thus we conclude that the maximal number of resolvable damped oscillations with this signal to noise level is 35. The parameter estimation is still a time consuming trial and error process, which could probably be automated.

A complete overview of all estimated DOAS and phases is given in Figure S 9, and a selection thereof in Figure 6. The averaging over four consecutive wavelengths results in a variance reduction, compare Figure 6 and Figure S 10. The estimated eigenfrequency and damping parameters are collated in Table II. Eight DOAS with damping rates above 20 ps^{-1} were needed to fit the coherent artefact or cross-phase modulation (XPM) (#26-31, #34 and #35 in Figure S 9P-U). These will not be discussed any further. Special are the two reverse DOAS (#32 and #33 in Figures 6(v)-6(x)) which are similar to free induction decays, resulting from a probe pulse that precedes the pump pulse, cf., Figure S 11.[26,59] In the data, these are obvious as low frequency oscillations extending before time zero (Figure 3). They are mainly described by the black DOAS32, with a frequency of 406 cm^{-1}, and damping rate of 39 ps^{-1}, which has its largest amplitude above 670 nm (black in Figure 6(w)). The origin of DOAS25 is unclear (black in Figure S 9P-R). Thus the oscillatory signal well after the IRF and XPM is described by 24 DOAS. Of these 24, four selected DOAS are depicted in Figures 6(c)-6(i). The most slowly decaying (0.9 ps^{-1}) is DOAS15 (green in Figures 6(c)-6(f)), with a frequency of 663 cm^{-1}. The DOAS #2 and #6 with frequencies of 1585 and 1235 cm^{-1} (blue and red in Figures 6(g)-6(i)) both show amplitude above 670 nm, where ESA dominates the SADS. They can thus be attributed to the electronically excited states. In DOAS2 and DOAS6, a node is accompanied by a phase jump at, respectively, 626.5 nm (indicated by the grey vertical lines in Figures 6(h) and 6(i)) and ≈633 nm. This corroborates that the presence of a node is a cancellation that occurs at the minimum of a potential energy surface, here of the excited state[18,25–27] and see our simulations below. A trend appears to be present in Figures 6(k), 6(n), 6(o), and 6(t), that the amplitude above 670 nm is highest for the DOAS 1-5, a bit smaller with DOAS 6-10, and very small for DOAS 11-24. The DOAS present very clear nodes in the emission wavelength (640 nm) for DOAS 5-12 and DOAS 14-24, with corresponding phase changes in the accompanying phase profiles.

Comparing to the population profiles, with the fastest equilibration rate constant of 0.82 ps^{-1} (cf., Figures 5(a) and 6(a)), and initial populations of all four species, it is not easily possible to associate the DOAS to species. Due to the ubiquitous presence of the node at the emission frequency of the terminally emitting PCB molecule, these oscillations can at least be attributed to that chromophore. Though there is likely additional amplitude from contributions of the other PCB molecules in the region. The DOAS amplitudes are relatively small near 580 nm, the DBV absorption maximum that corresponds to the bleach of the black species. This is probably caused by the pump pulse not having enough excess energy (cf., Figure 2) to excite many higher vibrational states of this species. The dominating contribution to this signal is then the ground state bleach, which does not exhibit pronounced oscillations (see Figure 3, Figure S 6, and below).

TABLE II. Estimated DOAS parameters of PC612: area (divided by γ_n), eigenfrequency ω_n (in cm^{-1}), and damping rate γ_n (in ps^{-1}) and provisional assignment. The errors estimated from the nonlinear least squares fit are a lower bound. These errors are huge for the coherent artefact related parameters. A zero error indicates that the parameter was kept fixed.

	Area/γ_n	ω_n	Error	γ_n	Error	Comment
DOAS1	10	1649.0	0.4	2.06	0.08	
DOAS2	33	1585.2	0.2	2.98	0.03	Figures 6(g)–6(i)
DOAS3	8	1466.3	0.8	3.97	0.15	
DOAS4	16	1372.9	0.9	3.16	0.16	
DOAS5	21	1348.7	0.6	2.94	0.11	
DOAS6	16	1235.5	0.2	2.05	0.04	Figures 6(g)–6(i)
DOAS7	9	1077.6	0.9	3.92	0.18	
DOAS8	15	1047.3	0.3	1.18	0.05	Figures 6(d)–6(f)
DOAS9	10	971.5	0.5	2.07	0.09	
DOAS10	60	880.9	4.2	11.97	0.79	
DOAS11	23	863.1	0.4	1.96	0.08	
DOAS12	65	823.5	3.9	10.65	0.78	
DOAS13	29	810.5	0.3	2.34	0.06	
DOAS14	13	697.0	0.8	2.86	0.15	
DOAS15	41	663.0	0.1	0.90	0.02	Figures 6(d)–6(f)
DOAS16	32	652.1	1.5	7.40	0.29	
DOAS17	20	515.4	0.3	2.44	0.07	
DOAS18	32	475.6	0.2	2.27	0.05	
DOAS19	28	417.1	1.2	6.49	0.24	
DOAS20	88	325.0	2.7	8.46	0.56	
DOAS21	36	319.2	1.1	3.32	0.22	
DOAS22	68	261.4	0.6	4.45	0.13	
DOAS23	35	227.8	0.7	3.80	0.12	
DOAS24	24	130.1	1.3	7.78	0.28	
DOAS25	355	10.0	0	12.14	0.17	Low frequency
DOAS26	1793	67.6	0	494.6	0	Coherent artefact
DOAS27	272	477.8	0	73.1	0	Coherent artefact
DOAS28	88	1230.4	0	147.6	0	Coherent artefact
DOAS29	590	1600.3	0	697.9	0	Coherent artefact
DOAS30	536	1626.9	0	829.6	0	Coherent artefact
DOAS31	5	1897.7	9.7	38.8	1.9	Coherent artefact
DOAS32	64	406.0	8.0	39.5	1.8	Reverse
DOAS33	17	1478.8	7.5	59.1	1.6	Reverse
DOAS34	1620	742.0	0	68.0	0	Coherent artefact
DOAS35	1525	757.2	0	66.5	0	Coherent artefact

SIMULATIONS

In order to connect the fitted DOAS parameters with the actual system coherent evolution, the dynamics of a vibrational wavepacket was simulated and analyzed in the same way as the experimental data. In the past, many efficient theoretical methods were developed for the description of transient absorption experiments. The typical examples are variants of the doorway-window picture.[60–62] In this work, we choose

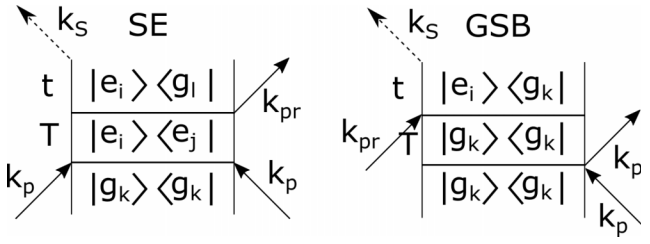

FIG. 7. Double-sided Feynman diagrams used for calculating the simulated transient absorption signal, left: SE and right: GSB. The system starts in canonical equilibrium given by the Boltzmann distribution of the population of the vibrational states in the ground state, g_k. The two interactions with the pump take the system out of the equilibrium. The coherence dynamics in the waiting time T results in the observed oscillations, and the oscillation frequency is given by the energy difference of the constituent states. The optical coherence evolution in emission time t determines the spectral position of the pathway in the transient absorption spectrum.

for the sake of simplicity a somewhat more direct approach in the form of response functions. Although impractical for the calculation of larger systems and/or finite pulses, the advantage of our approach is that it enables to directly follow the state of the system responding to the interaction with the light. As we will see further on, it also enables to correlate the waiting-time oscillation frequency with the emission frequency. The employed theoretical description is detailed in Ref. 63. Briefly, one selected strong vibrational mode of interest is quantized and explicitly included into the system, while all the other vibrations of either the pigments or the protein/solvent are included in the vibrational bath. In this description, both the explicitly quantized vibrational mode and the electronic degrees of freedom are interacting with the bath and the interaction is treated within second-order perturbation theory. The evolution of optical coherences, yielding lineshapes, is expressed by cumulant expansion. The excited- and ground-state dynamics is calculated by time-independent Redfield theory. The transient absorption signals were evaluated in an impulsive limit of ultrashort pulses.[62] In this limit, the two interactions with the pump pulse create an initial condition for the waiting time evolution in the excited and ground state. The interaction of the probe then causes emission of the signal in the probe direction. The double-sided Feynman diagrams used for the calculation of the simulated transient absorption signals are depicted in Figure 7.

The goal of the simulations is not to quantitatively reproduce the experimental data, but rather to qualitatively describe features present in the fitted DOAS and connect them to the physical properties of the system studied. To achieve this, we calculate separately the stimulated emission (SE) and ground state bleach (GSB) signals for a single pigment. To ease the comparison with the experiment, we choose the zero-phonon line at 16 450 cm^{-1} (608 nm) and the explicit vibrational frequency 662 cm^{-1} (about 25 nm in the spectral range considered). We use an overdamped Brownian oscillator to describe the bath spectral density,[62] with the bath correlation time of 50 fs and the coupling to the bath in order to obtain vibrational relaxation on the order of 100 fs and a lineshape width of 200 cm^{-1} (about 8 nm). The calculation is at room temperature and the initial equilibrium state before interaction with the pump is a canonical Boltzmann distribution in the ground state. The simulated transient absorption signals can be found in Figure S 12. Note that because of the 10 fs sampling interval of the emission time t these data are periodic in the frequency domain with 3333 cm^{-1}. Already from the unprocessed data, we can clearly see that in the SE signal the excited state dynamics including vibrational relaxation and coherent vibrational wavepacket oscillations is dominating. In the GSB signal, however, the vibrational wavepacket is not displaced by the two interactions with the ultrashort pump. Therefore there is no vibrational relaxation and in the impulsive limit also no coherent oscillations. Mathematically, this can be seen by using perturbation theory in the interaction with the light and realizing that in the Condon approximation the transition dipole moment operator is independent of the vibrational degrees of freedom. The two interactions with the light from one side, see Fig. 7 right, then leave the system in the ground state equilibrium.[64] In reality, this strictly applies when the duration of the pulse is shorter than the oscillation period of the vibration. In a real experiment with ultrashort pulses, the amplitude of the GSB oscillations will be strongly suppressed. The global SADS and DOAS of the simulated SE signals can be found in Figure 8. In the SE data, the intramolecular vibrational energy relaxation is described by a sequential kinetic scheme with increasing lifetimes, the populations of the species are shown in Figure 8(a). In the shape of the SADS the vibrational progression is clearly visible (Figures 8(a) and 8(b)), the peaks being a vibrational frequency apart.

Let us now focus on the origin of the oscillations. Since the energy relaxation dynamics is described by the sequential model and the SADS, the remaining DOAS evolution should reflect the coherent dynamics of the wavepacket. A vibrational wavepacket is a coherent superposition of the vibrational states; the fixed phase relation between its individual components holds it together. The observed oscillations, fitted by the damped cosines, are caused by the evolution of the coherences of this superposition. These coherences oscillate with a frequency equal to the energy difference between the constituent states, that is, with a multiple of the vibrational frequency. This can also clearly be seen from the double-sided Feynman diagrams in Fig. 7. The oscillation decay rate is given both by decoherence and by the wavepacket relaxation. At this point, we would like to note that because of the bath memory and coherence transfer, the decay of the coherences is not necessarily exponential. Then a single coherence decay will be fitted with multiple exponential components with the same DOAS shape, oscillation frequency, and different damping rates. This is probably the case of DOAS #6 and #7 in the SE, see Figures 8(g)-8(i). Because of this the number of resolved DOAS does not correspond to the number of coherences present. Generally the extracted frequencies indeed correspond (within the fitting error) to the vibrational frequency and its second and third harmonic, cf., Figures 8(d)-8(f), demonstrating the power of the DOAS to resolve the vibrations of the molecular system.

Considering the shape and phase of the DOAS, in the SE the DOAS peaks are found both at the SADS peak position of the transitions and around these peaks. In the latter case, in

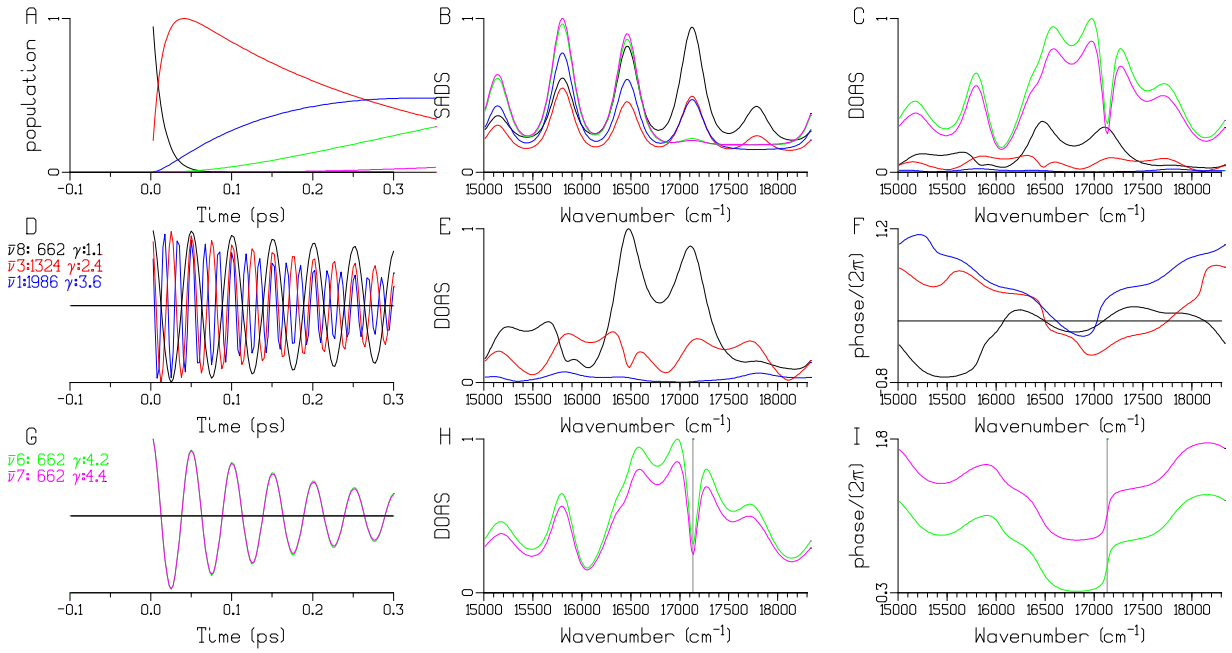

FIG. 8. Global fits of the simulated SE signals. (a) Evolution of species populations, (b) associated SADS, (c) five selected DOAS. (d) and (g) Cosine oscillations with frequencies $\bar{\nu}n$ (in cm^{-1}) (where n is the DOAS number) and damping rates γ (in 1 ps^{-1}) written in the legend at the left, using the appropriate color. (e) and (h) Estimated DOAS, color coded as in (d) and (g). (f) and (i) Accompanying phase profiles. The grey vertical lines at 17 135 cm^{-1} in panels (h) and (i) are discussed in the text.

the DOAS shape there are sharp nodes present at the position of the SADS peaks (e.g., indicated by the grey vertical line at 17 135 cm^{-1} in Figure 8(h) for DOAS #6 and #7, green and magenta). The phase exhibits abrupt changes, with π jumps at the position of the sharp nodes (e.g., indicated by the grey vertical line at 17 135 cm^{-1} in Figure 8(i) of the phase of DOAS #6 and #7, green and magenta). The presence of such phase jumps and sharp nodes at the position of the transitions is of special interest, as these have been reported before.[18,25–27] Our results correspond to those in Fig. 4(c) from Ref. 27 and in Fig. 7 from Ref. 25 and are consistent with Ref. 26. Most interestingly, in accordance with the simulation results, these features can be ascribed to the excited state. The presence of such features can thus be regarded as a signature of the excited state dynamics.

Finally, let us compare the DOAS features in the experimental, Figure 6, and simulated, Figure 8, data. In the experimental DOAS shapes and phases, we can see both of the features described above. In DOAS #15 (green in Figures 6(c)-6(f)) the peaks correspond to the vibrational progression, being about 662 cm^{-1} apart. This DOAS thus has the same features as the simulated DOAS #8 in the SE (black in Figures 8(c)-8(f)). In contrast, in experimental DOAS #2 (blue in Figures 6(g)-6(i)) the peaks are not separated by the vibrational frequency and there is a sharp node present at the position of the transition at 625 nm. The phase exhibits a rapid jump at the position of the node. This DOAS thus corresponds to the simulated DOAS #6 and #7 (green and magenta in Figures 8(c)-8(f)), with the node and phase jump at 17 135 cm^{-1}. Similar correspondences can be found for other experimental and simulated DOAS. This provides the desired connection between the DOAS and actual vibrational wavepacket dynamics. The presence of sharp nodes and phase jumps, together with the large oscillation amplitude (relative to the absolute signal), indicates that the oscillations originate from the excited state.

DISCUSSION

The long lived species that was mentioned in the *Transient absorption measurements* section is depicted in grey in Figure S 4. It shows a bleach at ≈650 nm, which corresponds to the red edge of the absorption spectrum. Thus it could correspond to a long-lived charge-transfer state that is directly excited by the broadband pulse. The putative bleach extends until the end of our measurement range, 715 nm. From 590 to 650 nm the shape of the grey SADS resembles the shape of the three PCB SADS. Below 590 nm absorption is present. Alternatively, the long lived species could correspond to accumulated triplets. In the 7.5 ps DADS (red in Figure 4) there is a net loss of bleach of excited states near 625 nm. Probably, in a small fraction of the complexes (≈9%), singlets annihilate with the long lived states. In the target analysis this loss is now visible as a smaller amplitude of the blue SADS relative to the red SADS (Figure 5(c)). Thus the timescale of this annihilation (in ≈9% of the complexes) is comparable to that of the 7.5 ps equilibration taking place in all PC612 complexes.

The frequencies of the DOAS with the damping rates smaller than 15 ps^{-1} most probably correspond to properties of the molecular system. DOAS with faster damping rates were required to fit XPM and IRF properties until about 50 fs after the maximum of the IRF. Compared to earlier studies[25,27] more than twice as many frequencies have been resolved. This is possible through the model based analysis of

these very high quality data. The IRF was 21 fs FWHM, and the pulse possessed a large power until 715 nm (Figure 2). Thus we could easily resolve frequencies up to ≈1600 cm^{-1}. The highest frequencies resolved in earlier studies were only ≈800 cm^{-1}.

The DOAS are analogous to DADS and can be directly interpreted as the amplitude of a given coherent oscillation, with a defined phase and dephasing lifetime, as a function of detection wavelength. While these are global lifetimes and cannot necessarily be assigned to a particular species, excluding the possibility of vibrational coherence across multiple chromophores, it is likely that each DOAS resolves oscillations fixed to a particular chromophore. The DOAS reveal clearly visible nodes, with corresponding phase change, that flag the minimum of the potential energy surface. This location is where, due to interference effects, oscillations cancel.[26]

Previously, Fourier transform maps of the dataset well after the IRF were used to identify oscillations and their phase character. In addition to resolving significantly more oscillations, at the frequencies that characterize the system, the DOAS method very clearly reveals the unique nodal features, phase profiles, and dephasing times for each of them. This represents the most detailed and complete analysis of vibrational coherence in a phycobiliprotein, fit simultaneously with its population dynamics, in the time domain from complete transient absorption datasets.

The placement of nodes in the data allows certain assignments of the DOAS in the excited state potential energy surface of individual chromophores. Nodes present at the emission wavelength of the complete complex indicate that the DOAS likely belongs to the terminally emitting PCB chromophore. In a complex with eight chromophores, this may not be possible to resolve. However, for those DOAS that have nodes to the blue of 640 nm, we can rely on the amplitude in the ESA region of the spectrum to assign them to the excited state. Overall we can see that excited state coherences are exclusively generated, as expected from impulsive excitation with a broadband pulse that covers the entire absorption spectrum of the complex.[22,24]

The comparison of our DOAS global fit with the previous results and the theoretical simulations well demonstrates the power of our analysis to resolve the frequencies present in the system. Recently there has been a growing interest in transient oscillations in nonlinear spectroscopy of pigment-protein complexes.[63,65–69] A particular emphasis is being put on distinguishing purely vibrational, excitonic, and mixed (vibronic) coherences and on assigning the oscillating spectral features to specific dynamic events, for instance, in photosynthetic energy transfer and charge separation.[39] The DOAS analysis can prove to be a valuable tool, as the estimated eigenfrequencies can be compared to known vibrations, elucidating the character of the coherences, while the unique spectral features can attribute them to the electronic excited state.

By global fit alone of the experimental data it is difficult, if not impossible, to interpret in detail the underlying dynamics. At the same time by a theoretical simulation it is unfeasible to directly fit the data already for moderately complex systems. Our DOAS analysis thus provides a useful "middle ground" where the theoretical description and fit of experimental data can meet.

CONCLUSIONS

The methodology presented here provides a complete description of the time evolution of the electronically and vibrationally excited states. No data are left out, and the IRF is fully taken into account. Thus from a huge amount of data interpretable parameters are estimated, describing the equilibration of electronically excited states (Figure 5) and the damped oscillations (cf., Figure 6 and Table II). The DOAS are expressing the most important vibrational frequencies present in the molecular system estimated from a simultaneous, global and target analysis of *three complete data sets*. The simultaneous analysis of multiple datasets is mandatory to distinguish signal and noise, and with the help of residual analysis establish the amount of oscillations needed to describe the complete data (Figure S 7 and Figure S 8). The DOAS methodology is applicable to broadband transient absorption of both simple and complex systems.

SUPPLEMENTARY MATERIAL

See supplementary material for thirteen figures demonstrating the reproducibility of the data and the quality of the fit, the analysis of the residuals, and the complete DOAS analysis of the data and of the simulations. In addition, the effect of averaging over four consecutive wavelengths is demonstrated.

ACKNOWLEDGMENTS

We thank Jürgen Hauer and Tomáš Mančal for helpful discussions. I.H.M.v.S., P.M., and R.v.G. were supported by an Advanced Investigator grant to R.v.G. from the European Research Council (Grant No. 267333, PHOTPROT). P.M., R.v.G., and G.D.S. acknowledge the Canadian Institute For Advanced Research (CIFAR). C.C.J. acknowledges funding for her doctoral studies from NSERC Canada Graduate Scholarships and the University of Toronto. J.J.S. acknowledges funding from the European Union's Horizon 2020 research and innovation programme under Grant Agreement No. 654148 Laserlab-Europe. G.D.S. acknowledges the United States Air Force Office of Scientific Research (Grant No. FA9550-13-1-0005). R.v.G. gratefully acknowledges his Academy Professorship from the Netherlands Royal Academy of Sciences (KNAW).

[1]S. L. Dexheimer, Q. Wang, L. A. Peteanu, W. T. Pollard, R. A. Mathies, and C. V. Shank, "Femtosecond impulsive excitation of nonstationary vibrational states in bacteriorhodopsin," Chem. Phys. Lett. **188**, 61–66 (1992).
[2]D. Polli, M. R. Antognazza, D. Brida, G. Lanzani, G. Cerullo, and S. De Silvestri, "Broadband pump-probe spectroscopy with sub-10-fs resolution for probing ultrafast internal conversion and coherent phonons in carotenoids," Chem. Phys. **350**, 45–55 (2008).
[3]A. H. Zewail, "Femtochemistry: Atomic-scale dynamics of the chemical bond," J. Phys. Chem. A **104**, 5660–5694 (2000).

[4]M. Liebel and P. Kukura, "Broad-band impulsive vibrational spectroscopy of excited electronic states in the time domain," J. Phys. Chem. Lett. **4**, 1358–1364 (2013).
[5]J. C. Dean, S. Rafiq, D. G. Oblinsky, E. Cassette, C. C. Jumper, and G. D. Scholes, "Broadband transient absorption and two-dimensional electronic spectroscopy of methylene blue," J. Phys. Chem. A **119**, 9098–9108 (2015).
[6]S. Rafiq and G. D. Scholes, "Slow intramolecular vibrational relaxation leads to long-lived excited-state wavepackets," J. Phys. Chem. A **120**, 6792–6799 (2016).
[7]J. Brazard, L. A. Bizimana, T. Gellen, W. P. Carbery, and D. B. Turner, "Experimental detection of branching at a conical intersection in a highly fluorescent molecule," J. Phys. Chem. Lett. **7**, 14–19 (2016).
[8]M. H. Vos, J. C. Lambry, S. J. Robles, D. C. Youvan, J. Breton, and J. L. Martin, "Direct observation of vibrational coherence in bacterial reaction centers using femtosecond absorption spectroscopy," Proc. Natl. Acad. Sci. U. S. A. **88**, 8885–8889 (1991).
[9]D. M. Jonas, M. J. Lang, Y. Nagasawa, T. Joo, and G. R. Fleming, "Pump–probe polarization anisotropy study of femtosecond energy transfer within the photosynthetic reaction center of rhodobacter sphaeroides R26," J. Phys. Chem. **100**, 12660–12673 (1996).
[10]S. Lin, A. K. W. Taguchi, and N. W. Woodbury, "Excitation wavelength dependence of energy transfer and charge separation in reaction centers from rhodobacter Sphaeroides: Evidence for adiabatic electron transfer," J. Phys. Chem. **100**, 17067–17078 (1996).
[11]S. Savikhin, Y. Zhu, S. Lin, R. E. Blankenship, and W. S. Struve, "Femtosecond spectroscopy of chlorosome antennas from the green photosynthetic bacterium chloroflexus aurantiacus," J. Phys. Chem. **98**, 10322–10334 (1994).
[12]S. Savikhin, D. R. Buck, and W. S. Struve, "Oscillating anisotropies in a bacteriochlorophyll protein: Evidence for quantum beating between exciton levels," Chem. Phys. **223**, 303–312 (1997).
[13]M. Chachisvilis, T. Pullerits, M. R. Jones, C. N. Hunter, and V. Sundström, "Vibrational dynamics in the light-harvesting complexes of the photosynthetic bacterium rhodobacter sphaeroides," Chem. Phys. Lett. **224**, 345–354 (1994).
[14]W. M. Diffey, B. J. Homoelle, M. D. Edington, and W. F. Beck, "Excited-state vibrational coherence and anisotropy decay in the bacteriochlorophyll a dimer protein B820," J. Phys. Chem. B **102**, 2776–2786 (1998).
[15]E. J. Heller, "The semiclassical way to molecular spectroscopy," Acc. Chem. Res. **14**, 368–375 (1981).
[16]R. B. Bernstein and A. H. Zewail, "Femtosecond real-time probing of reactions. III. Inversion to the potential from femtosecond transition-state spectroscopy experiments," J. Chem. Phys. **90**, 829–842 (1989).
[17]C. Cohen-Tannoudji, B. diu, and F. Lalöo, *Quantum Mechanics* (Wiley-Interscience, Paris, 1977).
[18]M. H. Vos, F. Rappaport, J.-C. Lambry, J. Breton, and J.-L. Martin, "Visualization of coherent nuclear motion in a membrane protein by femtosecond spectroscopy," Nature **363**, 320–325 (1993).
[19]I. A. Walmsley, F. W. Wise, and C. L. Tang, "On the difference between quantum beats in impulsive stimulated Raman scattering and resonance Raman scattering," Chem. Phys. Lett. **154**, 315–320 (1989).
[20]C. J. Bardeen, Q. Wang, and C. V. Shank, "Femtosecond chirped pulse excitation of vibrational wave packets in Ld690 and bacteriorhodopsin," J. Phys. Chem. A **102**, 2759–2766 (1998).
[21]C. J. Bardeen, Q. Wang, and C. V. Shank, "Selective excitation of vibrational wave packet motion using chirped pulses," Phys. Rev. Lett. **75**, 3410–3413 (1995).
[22]D. M. Jonas, S. E. Bradforth, S. A. Passino, and G. R. Fleming, "Femtosecond wavepacket spectroscopy: Influence of temperature, wavelength, and pulse duration," J. Phys. Chem. **99**, 2594–2608 (1995).
[23]W. Pollard and R. Mathies, "Analysis of femtosecond dynamic absorption spectra of nonstationary states," Annu. Rev. Phys. Chem. **43**, 497–523 (1992).
[24]A. S. Johnson, J. Yuen-Zhou, A. Aspuru-Guzik, and J. J. Krich, "Practical witness for electronic coherences," J. Chem. Phys. **141**, 244109 (2014).
[25]P. C. Arpin *et al.*, "Spectroscopic studies of cryptophyte light harvesting proteins: Vibrations and coherent oscillations," J. Phys. Chem. B **119**, 10025–10034 (2015).
[26]J. A. Cina, P. A. Kovac, C. C. Jumper, J. C. Dean, and G. D. Scholes, "Ultrafast transient absorption revisited: Phase-flips, spectral fingers, and other dynamical features," J. Chem. Phys. **144**, 175102 (2016).
[27]S. D. McClure, D. B. Turner, P. C. Arpin, T. Mirkovic, and G. D. Scholes, "Coherent oscillations in the Pc577 cryptophyte antenna occur in the excited electronic state," J. Phys. Chem. B **118**, 1296–1308 (2014).
[28]S. Rafiq, J. C. Dean, and G. D. Scholes, "Observing vibrational wavepackets during an ultrafast electron transfer reaction," J. Phys. Chem. A **119**, 11837–11846 (2015).
[29]Q. Wang, R. W. Schoenlein, L. A. Peteanu, R. A. Mathies, and C. V. Shank, "Vibrationally coherent photochemistry in the femtosecond primary event of vision," Science **266**, 422 (1994).
[30]F. Novelli, A. Nazir, G. H. Richards, A. Roozbeh, K. E. Wilk, P. M. G. Curmi, and J. A. Davis, "Vibronic resonances facilitate excited-state coherence in light-harvesting proteins at room temperature," J. Phys. Chem. Lett. **6**, 4573–4580 (2015).
[31]F. D. Fuller, J. Pan, A. Gelzinis, V. Butkus, S. S. Senlik, D. E. Wilcox, C. F. Yocum, L. Valkunas, D. Abramavicius, and J. P. Ogilvie, "Vibronic coherence in oxygenic photosynthesis," Nat. Chem. **6**, 706–711 (2014).
[32]L. Viani, M. Corbella, C. Curutchet, E. J. O'Reilly, A. Olaya-Castro, and B. Mennucci, "Molecular basis of the exciton–phonon interactions in the Pe545 light-harvesting complex," Phys. Chem. Chem. Phys. **16**, 16302–16311 (2014).
[33]A. Kolli, E. J. O'Reilly, G. D. Scholes, and A. Olaya-Castro, "The fundamental role of quantized vibrations in coherent light harvesting by cryptophyte algae," J. Chem. Phys. **137**, 174109 (2012).
[34]E. J. O'Reilly and A. Olaya-Castro, "Non-classicality of the molecular vibrations assisting exciton energy transfer at room temperature," Nat. Commun. **5**, 3012 (2014).
[35]A. Chin, J. Prior, R. Rosenbach, F. Caycedo-Soler, S. Huelga, and M. Plenio, "The role of non-equilibrium vibrational structures in electronic coherence and recoherence in pigment-protein complexes," Nat. Phys. **9**, 113–118 (2013).
[36]A. Chenu, N. Christensson, H. F. Kauffmann, and T. Mančal, "Enhancement of vibronic and ground-state vibrational coherences in 2d spectra of photosynthetic complexes," Sci. Rep. **3**, 2029 (2013).
[37]J. M. Womick and A. M. Moran, "Vibronic enhancement of exciton sizes and energy transport in photosynthetic complexes," J. Phys. Chem. B **115**, 1347–1356 (2011).
[38]V. Tiwari, W. K. Peters, and D. M. Jonas, "Electronic resonance with anti-correlated pigment vibrations drives photosynthetic energy transfer outside the adiabatic framework," Proc. Natl. Acad. Sci. U. S. A. **110**, 1203–1208 (2013).
[39]V. I. Novoderezhkin, E. Romero, and R. van Grondelle, "How exciton-vibrational coherences control charge separation in the photosystem II reaction center," Phys. Chem. Chem. Phys. **17**, 30828–30841 (2015).
[40]A. Halpin, J. M. JohnsonPhilip, R. Tempelaar, R. S. Murphy, J. Knoester, L. C. JansenThomas, and R. J. D. Miller, "Two-dimensional spectroscopy of a molecular dimer unveils the effects of vibronic coupling on exciton coherences," Nat. Chem. **6**, 196–201 (2014).
[41]S. Ruetzel, M. Diekmann, P. Nuernberger, C. Walter, B. Engels, and T. Brixner, "Photoisomerization among ring-open merocyanines. I. Reaction dynamics and wave-packet oscillations induced by tunable femtosecond pulses," J. Chem. Phys. **140**, 224310 (2014).
[42]T. S. Rose, M. J. Rosker, and A. H. Zewail, "Femtosecond real-time observation of wave packet oscillations (resonance) in dissociation reactions," J. Chem. Phys. **88**, 6672–6673 (1988).
[43]U. Banin, A. Waldman, and S. Ruhman, "Ultrafast photodissociation of I3–in Solution: Direct observation of coherent product vibrations," J. Chem. Phys. **96**, 2416–2419 (1992).
[44]S. De Silvestri, J. Fujimoto, E. Ippen, E. B. Gamble, L. R. Williams, and K. A. Nelson, "Femtosecond time-resolved measurements of optic phonon dephasing by impulsive stimulated Raman scattering in α-perylene crystal from 20 to 300 K," Chem. Phys. Lett. **116**, 146–152 (1985).
[45]A. Weiner, D. Leaird, G. P. Wiederrecht, and K. A. Nelson, "Femtosecond pulse sequences used for optical manipulation of molecular motion," Science **247**, 1317–1319 (1990).
[46]H. Zeiger, J. Vidal, T. Cheng, E. Ippen, G. Dresselhaus, and M. Dresselhaus, "Theory for displacive excitation of coherent phonons," Phys. Rev. B **45**, 768 (1992).
[47]M. Liebel, C. Schnedermann, T. Wende, and P. Kukura, "Principles and applications of broadband impulsive vibrational spectroscopy," J. Phys. Chem. A **119**, 9506–9517 (2015).
[48]S. J. Harrop *et al.*, "Single-residue insertion switches the quaternary structure and exciton states of cryptophyte light-harvesting proteins," Proc. Natl. Acad. Sci. U. S. A. **111**, E2666–E2675 (2014).
[49]V. I. Novoderezhkin, A. B. Doust, C. Curutchet, G. D. Scholes, and R. van Grondelle, "Excitation dynamics in phycoerythrin 545: Modeling of

steady-state spectra and transient absorption with modified redfield theory," Biophys. J. **99**, 344–352 (2010).
[50]C. Curutchet, V. I. Novoderezhkin, J. Kongsted, A. Muñoz-Losa, R. van Grondelle, G. D. Scholes, and B. Mennucci, "Energy flow in the cryptophyte Pe545 antenna is directed by bilin pigment conformation," J. Phys. Chem. B **117**, 4263–4273 (2013).
[51]I. H. M. van Stokkum, D. S. Larsen, and R. van Grondelle, "Erratum to "global and target analysis of time-resolved spectra"," Biochim. Biophys. Acta **1658**, 262 (2004).
[52]I. H. M. van Stokkum, D. S. Larsen, and R. van Grondelle, "Global and target analysis of time-resolved spectra," Biochim. Biophys. Acta **1657**, 82–104 (2004).
[53]A. R. Holzwarth, "Data analysis of time-resolved measurements," in *Biophysical Techniques in Photosynthesis*, edited by J. Amesz and A. J. Hoff (Kluwer, Dordrecht, The Netherlands, 1996), pp. 75–92.
[54]G. H. Golub and R. J. LeVeque, *Extensions and Uses of the Variable Projection Algorithm for Solving Nonlinear Least Squares Problems* (Proc. of the 1979 Army Numerical Analysis and Comp. Conf., ARO Report 79-3, 1979), pp. 1–12.
[55]J. F. Nagle, "Solving complex photocycle kinetics—Theory and direct method," Biophys. J. **59**, 476–487 (1991).
[56]K. M. Mullen and I. H. M. van Stokkum, "The variable projection algorithm in time-resolved spectroscopy, microscopy and mass spectrometry applications," Numer. Algorithms **51**, 319–340 (2009).
[57]G. J. Wedemayer, D. G. Kidd, D. E. Wemmer, and A. N. Glazer, "Phycobilins of cryptophycean algae. Occurrence of dihydrobiliverdin and mesobiliverdin in cryptomonad biliproteins," J. Biol. Chem. **267**, 7315–7331 (1992), available at http://www.jbc.org/content/267/11/7315.full.pdf?sid=d1ba29c8-f3da-43ef-9298-af0d6e88d95f.
[58]R. Tasler, T. Moises, and N. Frankenberg-Dinkel, "Biochemical and spectroscopic characterization of the bacterial phytochrome of pseudomonas aeruginosa," FEBS J. **272**, 1927–1936 (2005).
[59]P. Hamm and M. Zanni, *Concepts and Methods of 2d Infrared Spectroscopy* (Cambridge University Press, 2011).
[60]A. T. N. Kumar, F. Rosca, A. Widom, and P. M. Champion, "Investigations of ultrafast nuclear response induced by resonant and nonresonant laser pulses," J. Chem. Phys. **114**, 6795–6815 (2001).
[61]A. T. N. Kumar, F. Rosca, A. Widom, and P. M. Champion, "Investigations of amplitude and phase excitation profiles in femtosecond coherence spectroscopy," J. Chem. Phys. **114**, 701–724 (2001).
[62]S. Mukamel, *Principles of Nonlinear Optical Spectroscopy* (Oxford University Press on Demand, 1999).
[63]P. Malý, O. J. G. Somsen, V. I. Novoderezhkin, T. Mančal, and R. van Grondelle, "The role of resonant vibrations in electronic energy transfer," ChemPhysChem **17**, 1356–1368 (2016).
[64]C. N. Lincoln, J. Hayden, A. G. Pour, V. Perlík, F. Šanda, and J. Hauer, "A quantitative study of coherent vibrational dynamics probed by heterodyned transient grating spectroscopy," Vib. Spectrosc. **85**, 167–174 (2016).
[65]M. B. Plenio, J. Almeida, and S. F. Huelga, "Origin of long-lived oscillations in 2d-Spectra of a quantum vibronic model: Electronic versus vibrational coherence," J. Chem. Phys. **139**, 235102 (2013).
[66]E. Romero, R. Augulis, V. I. Novoderezhkin, M. Ferretti, J. Thieme, D. Zigmantas, and R. van Grondelle, "Quantum coherence in photosynthesis for efficient solar-energy conversion," Nat. Phys. **10**, 676–682 (2014).
[67]F. Fassioli, R. Dinshaw, P. C. Arpin, and G. D. Scholes, "Photosynthetic light harvesting: Excitons and coherence," J. R. Soc. Interface **11**, 20130901 (2014).
[68]A. Chenu and G. D. Scholes, "Coherence in energy transfer and photosynthesis," Annu. Rev. Phys. Chem. **66**, 69–96 (2015).
[69]Y.-C. Cheng and G. R. Fleming, "Dynamics of light harvesting in photosynthesis," Phys. Chem. **60**, 241 (2009).
[70]After the submission of our manuscript we learned that an alternative approach to globally fit damped oscillations was developed independently and simultaneously by S. Schott, L. Ress, J. Hrušák, P. Nuernberger, and T. Brixner (submitted) *Identification of photofragmentation patterns in trihalide anions by global analysis of vibrational wavepacket dynamics in broadband transient absorption data*.